RSC Advances

PAPER

View Article Online
View Journal | View Issue

Cite this: *RSC Adv.*, 2020, **10**, 15825

Doxorobicin as cargo in a redox-responsive drug delivery system capped with water dispersible ZnS nanoparticles

Lukáš Žid,[a] Vladimír Zeleňák, *[a] Vladimír Girman,[b] Jozef Bednarčík,[b] Adriana Zeleňáková,[b] Jaroslava Szűcsová,[b] Virginie Hornebecq,[c] Alexander Hudák,[d] Monika Šuleková[d] and Lucia Váhovská[d]

In this work, we have prepared and investigated a redox-responsive drug delivery system (DDS) based on a porous carrier. Doxorubicin (DOX), a chemotherapy medication for treatment of different kinds of cancer, was used as a model drug in the study. DOX was loaded in ordered hexagonal mesoporous silica SBA-15, a nanoporous material with good biocompatibility, stability, large pore size and specific surface area (S_{BET} = 908 m^2 g^{-1}, V_P = 0.79 cm^3 g^{-1}, d = 5.9 nm) and easy surface modification. To prepare the redox-responsive system, cystamine derivative ligands, with redox active disulphide linkers were grafted onto the surface of SBA-15. To ensure no significant premature release of DOX from the porous system, thioglycolic acid modified ZnS nanoparticles (ZnS–COOH NPs) were used as pore capping agents. The grafted redox-responsive cystamine derivative ligand containing disulphide linkers was bonded by a peptide bond to the thioglycolic acid groups of ZnS–COOH NPs, capping the pores. Once the disulphide bond was cleaved, the ZnS–COOH NPs caps were released and pores were opened to deliver the DOX cargo. The dithiol bond was cleavable by redox active molecules such as dithiothreitol (DTT) or glutathione, the concentration of which in cancer cells is 4 times higher than in healthy cells. The redox release of DOX was studied in two different media, physiological saline solution with DTT and saline without DTT. The prepared DDS proved the concept of redox responsive release. All samples were characterised by powder X-ray diffraction (XRD), transition electron microscopy (TEM), nitrogen adsorption/desorption at 77 K, Fourier-transform infrared spectroscopy (FTIR), thermal analysis and zeta potential measurements. The presence of semiconducting ZnS nanoparticle caps on the pore openings was detected by magnetic measurements using SQUID magnetometry showing that such cargo systems could be monitored using magnetic measurements which opens up the possibilities of using such drug delivery systems as theranostic agents.

Received 5th March 2020
Accepted 13th April 2020

DOI: 10.1039/d0ra02091e

rsc.li/rsc-advances

Introduction

For a few decades cancer treatment has been in the spotlight of research, however it is still the second most abundant cause of human death.[1] Many new drugs have been developed through the years, of which nearly 40% can be described as hydrophobic.[2] The interaction of the drugs with a body, which consists of 50 to 60% water, greatly influences their bioavailability. Drugs with low solubility in water only partially penetrate the gastrointestinal tract, which results in a higher dosage being needed to maintain the active concentration in a target tissue (therapeutic window).[3] Researchers have invented several ways to overcome the low water solubility of drugs. One promising way is represented by a so-called drug delivery systems (DDS). DDS are based on the idea that a drug can be masked or isolated in the body until it reaches the target site of action. Such a system should exhibit low leakage throughout the delivery process and release its cargo at a target site. The advanced DDS are designed and prepared to release the drug after some internal chemical stimulus such as pH,[4] overexpression of specific receptors,[5] the presence of enzymes,[6] redox agents,[7] up-regulation of certain enzymes,[8] *etc.* Moreover, a drug can be released or accumulated in a specific part of a body also by external physical stimuli, such as light,[9,10] microwave radiation,[11] ultrasound[12] or a magnetic field.[13] Currently, mesoporous silica nanoparticles (MSNs) DDS are very intensively studied.

[a]*Department of Inorganic Chemistry Faculty of Science, P. J. Šafárik University, Moyzesova 11, SK-041 54 Košice, Slovak Republic. E-mail: vladimir.zelenak@upjs.sk; Tel: +421552342343*

[b]*Institute of Physics, P. J. Šafárik University, Park Angelinum 9, 04001 Košice, Slovakia*

[c]*Aix Marseille Univ, CNRS, MADIREL, Marseille, France*

[d]*Department of Chemistry, Biochemistry and Biophysics, Institute of Pharmaceutical Chemistry, The University of Veterinary Medicine and Pharmacy in Košice, Košice 041 81, Slovak Republic*

In the present work we have designed a redox responsive DDS for doxorubicin (DOX) delivery. DOX (see Fig. 1) is a chemotherapy medication used to treat different types of cancer (leukemia, cancer of breast, lungs, stomach, soft tissues *etc.*). Doxorubicin is hydrophobic drug, which belongs to the group of anthracycline antibiotics with antineoplastic activity. It acts as DNA intercalator that inhibits topoisomerase II, therefore blocking the cancer cell growth.[14]

The DDS was prepared using thioglycolic acid modified ZnS nanoparticles as a gatekeeper attached to the surface of SBA-15 silica by organic linker containing dithiol bond. The dithiol bond is cleavable using redox molecules such as dithiothreitol or glutathione. It is well known that glutathione concentration in intracellular matrix is 100–1000 times larger compared to extracellular fluids. Moreover, cancer cells contain 4 times more glutathione than healthy cells, which ultimately leads to improved targeting of DOX and decreased incidence of side effects. In addition, the ZnS–COOH NPs are dispersible and biocompatible in biological systems with little to no toxicity in comparison to *e.g.* CdS quantum dots. Moreover, ZnS can also act as antioxidant with antibacterial and antifungal activity.[15]

The concept of combination of linker with disulphide bonds and metal-based nanoparticles as pore capping agents was already reported in the literature, *e.g.* by using CdS,[16] Fe_2O_3 [17] or Au[18,19] nanoparticles as pore blocking agents. However, as of now, not much research is available on disulphide linkers with ZnS based nanoparticles and such reports are relatively scarce,[20] especially for delivery of anticancer drugs. Research concerning mesoporous silica and ZnS nanoparticles was up till now more oriented to quantum size effects and optical properties of such materials.[21,22]

Materials and methods

Materials

All chemicals were used as purchased, without further purification. Tetraethyl orthosilicate 98% (TEOS), (3-chloropropyl) triethoxysilane 96% (CPTES), cystamine dihydrochloride 96%, D,L-dithiothreitol 98%, sodium sulfide nonahydrate trace metals basis, thioglycolic acid, zinc acetate dihydrate 99.999%, urea, *N*-(3-dimethylaminopropyl)-*N*′-ethylcarbodiimide hydrochloride 98% (EDC-HCl), *N*-hydroxysuccinimide 98% (NHS), dichloromethane, tetrahydrofurane (THF) and doxorubicin hydrochloride EP reference standard (DOX) were purchased from Sigma Aldrich company. Hydrochloric acid and ammonia solution were purchased from CentralChem. Dialysis was done using Servapor tubing with MW_{CO} 12000–14000.

The experimental synthetic works were conducted either according to the published literature procedures or, when modified or newly designed, the procedures were checked for reproducibility.

Preparation of ZnS–COOH nanoparticles

Water dispersible ZnS–COOH nanoparticles were prepared with a slight modification of the procedure presented by Liu *et al.*[23] Briefly, 0.66 g of $Zn(CH_3COO)_2 \cdot 2H_2O$ was dissolved in 25 mL of ultrapure water and 2.25 mL of thioglycolic acid was then slowly added into the solution. The solution was stirred for 10 min followed by addition of 2.16 g of $Na_2S \cdot 9H_2O$ previously dissolved in 5 mL of ultrapure water. Stirring continued until clear solution was obtained. Then, 2.5 mL of 0.9 M urea solution was added dropwise and the pH was adjusted to 9–10 with ammonia. The mixture was autoclaved in 50 mL Teflon lined flask for 2 hours at 150 °C. The autoclave was cooled down to room temperature, and the resulting product was isolated from reaction by-product by double dialysis against 500 mL of pure water. The product was denoted as ZnS–COOH.

Synthesis of SBA-15

SBA-15 was prepared by the procedure described in ref. 24. In the first step, the 30 mL of deionized water was mixed in a polyethylene (PE) flask with 120 g of 2 M HCl. Then, 4 g of Pluronic P-123 were added to the mixture and dissolved at 308 K under continuous stirring. After complete dissolution of surfactant, 8.5 g of TEOS were added dropwise and stirred for 20 hours at 308 K, followed by hydrothermal treatment at 353 K for 24 hours. Product was filtered off and thoroughly washed with deionized water. Final porous material was obtained by gentle heating (1 K min^{-1}) and calcination at 823 K for 7 hours.

Modification of SBA-15 by amino-disulphide moieties

In order to achieve redox responsive release, the disulphide bond was used as a part of a linker between SBA-15 and ZnS–COOH nanoparticles. Synthesis of redox responsive SBA-15 (rSBA-15) was done in 2 steps outlined in Fig. 2. In the first step, the SBA-15 was modified with 3-chloropropyl ligands by grafting. Briefly, 0.9 g of pre-dried SBA-15 (at 150 K) was dispersed in 50 mL of dry toluene in 3-neck flask under N_2 atmosphere. Mixture was stirred and then the 3 mL of CPTES were added, followed by the reflux for 24 hours. Modified silica was centrifuged and washed 3 times with toluene to remove

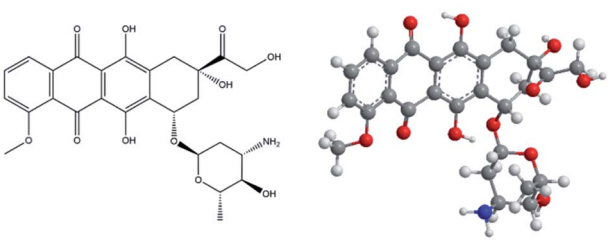

Fig. 1 Structural formula (left) and 3D model of doxorubicin (right); blue – nitrogen, red – oxygen, grey – carbon, white – hydrogen.

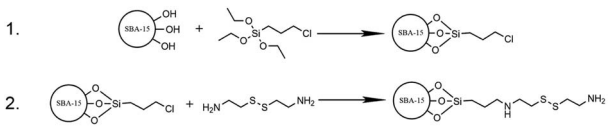

Fig. 2 Simplified representation of two-step preparation process for rSBA-15.

unreacted CPTES. Modified silica was left to dry at laboratory temperature. Second step of the reaction was done by amine alkylation (S_N2 reaction mechanism) in aprotic solvent (THF). Prior to the second step, the 0.5 g (2.22 mmol) of cystamine dihydrochloride was turned into free base form by neutralisation reaction with 0.195 g (4.88 mmol) of NaOH. The free base was isolated by extraction with dichloromethane. The water phase was discarded, and the organic phase was evaporated to give the yellow oily product – cystamine. The cystamine was mixed with 50 mL of THF and 500 mg of CPTES modified SBA-15. The mixture was refluxed for 24 hours and the product was filtered off and thoroughly washed with THF. Obtained white powder was denoted as rSBA-15.

Loading of SBA-15 with DOX and pore capping

DOX was loaded into the pores of rSBA-15 from its aqueous solution and capped with ZnS–COOH NPs by the 2-step process depicted in Fig. 3. In detail, 20 mg of DOX was dissolved in 20 mL of deionized water and 100 mg of rSBA-15 was added. The DOX was left to adsorb into the pores of rSBA-15 under stirring at laboratory temperature for 24 hours. 2 hours before the end of DOX adsorption step, the carboxylic groups of ZnS–COOH nanoparticles were activated in separate flask, to promote a peptide bond formation. The 50 mg of ZnS–COOH nanoparticles were added to the 20 mL of deionized water and the pH was adjusted to 5. Next, 40 mg of EDC-HCl and 25 mg of NHS were added. The mixture was stirred for 2 hours and then poured into the first flask with rSBA-15 and DOX to entrap the DOX inside the pores. The pH was adjusted to 8 and the mixture was stirred for 12 hours. Final product was filtered off and washed with deionized water. Product, denoted as DOX–rSBA-15, was dried at laboratory temperature and stored in a fridge.

In vitro drug release assay

To obtain the release profiles and redox sensitivity at 2 different media, the 20 mg of DOX–rSBA-15 was placed in Eppendorf tube and the 2 mL of release media were added. A physiological saline solution and physiological saline with DTT (10 mM) were used a release media. The samples were placed on a rotator (30 rpm) in incubator set at 37 °C. The sampling was done in predefined intervals from 1 to 48 hours. The concentration change was measured by UV-VIS spectroscopy. Obtained values were recalculated to release percent and plotted against time.

Characterization of samples

Adsorption/desorption of N_2 at 77 K was performed with Micromeritics ASAP 2020 plus instrument. The Brunauer–Emmett–Teller (BET) equation was used to obtain the specific surface area of prepared samples. The *t*-plot method was used to compute the pore volume, and Barret–Halenda–Joyner (BJH) method was used for pore size determination.

X-ray diffraction (XRD) experiments were performed in reflection mode with Bragg–Brentano parafocusing geometry using a Rigaku Ultima IV multipurpose diffractometer. X-ray lamp with Cu-Kα1,2 radiation (λ = 0.154 nm) was used. Powder samples were put on a glass sample holder. Diffracted photons were collected using a D/teX Ultra-high-speed, position-sensitive detector system by scanning 2θ range from 10° up to 90° with the step size of 0.02°.

TEM images were taken by JEOL TEM 2100F UHR microscope operated at 200 kV. The microscope was run in STEM-DF mode. All samples for TEM observation are supported on mesh copper grid and deposited by the holey carbon film. ImageJ software was used to obtain the particle size distribution of nanoparticles.[25]

FT-IR spectra were recorded with a Nicolet 6700 FT-IR spectrophotometer using KBr pellets with the sample/KBr mass ratio 1/100.

Thermal characterisation was used to determine the mass of loaded DOX, chemical groups bonded to the surface of SBA-15 and composition of ZnS–COOH nanoparticles. TGA analysis was carried out using STA Netzch 409 PC apparatus under dynamic conditions in air atmosphere with heating rate 9 °C min^{-1}.

Change in concentration during release experiment and analysis of ZnS–COOH NPs was measured with Specord 350 UV-VIS spectrophotometer (Analytic Jena). Three independent release measurements were made, and the respective value was obtained as an average of these measurements.

Zeta potential of the studied samples was estimated by DLS method (Dynamic Light Scattering) using a Zetasizer NANO-ZS (Malvern). Measurements were carried out at temperature 25 °C, using a dilute suspension of particles in an aqueous solution of pH = 7.4 and sonicated for 5 min before measurement. The respective zeta potential value was determined as an average of 40 scans. In software ZetaSizer Malvern, the Henry equation and Smoluchowski approximation were used to calculate zeta potential from particles mobility.

Magnetic properties were investigated using a SQUID (Superconducting Quantum Interference Device) magnetometer MPMS3 in the temperature range of 1.8–300 K and in the external dc fields up to 7 T. A powder sample was placed in a special polypropylene VSM capsule to avoid the contribution of the sample holder. Pascal's constants were subtracted from total susceptibility.

Diffraction profile analysis. Diffraction profile parameters such as Bragg peak intensity, position and width carry important information about the sample's microstructure. The peak position $2\theta_{hkl}$ is closely related with the lattice parameter a. The width of the Bragg reflection β_{hkl} contains useful information about the mean size of coherently scattering domains. In 1918 Scherrer[26] derived an equation which relates the mean (volume average) crystallite size D of a powder to the broadening $\beta_{hkl}{}^{D}$ of its powder diffraction peaks

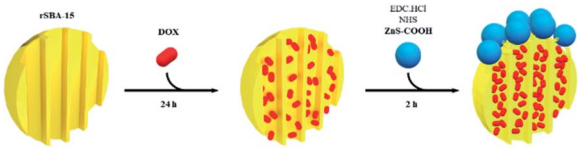

Fig. 3 Schematic preparation of DOX–rSBA-15.

$$\beta_{hkl}{}^{D} = \frac{K\lambda}{D\cos\theta_{hkl}} \quad (1)$$

where K is the Scherrer constant (in our calculation of grain sizes, K was equal to 0.9), λ is the wavelength of X-rays and θ_{hkl} is related to the position of the Bragg peak. It should be noted that the Scherrer eqn (1) as stated above ignores effects of strain on diffraction line broadening.

The Williams–Hall method[27] relies on the principle that the approximate formulae for size broadening $\beta_{hkl}{}^{D}$ and strain broadening $\beta_{hkl}{}^{\varepsilon}$ show different dependence on Bragg angle $2\theta_{hkl}$ and thus the total line broadening β_{hkl} can be expressed in the form

$$\beta_{hkl} = \beta_{hkl}{}^{\varepsilon} + \beta_{hkl}{}^{D} = C\varepsilon\tan\theta_{hkl} + \frac{K\lambda}{D\cos\theta_{hkl}} \quad (2)$$

where ε is the mean strain and C represents the constant, which depends on the assumptions made concerning the nature of the inhomogeneous strain but is typically equal to 4.[28] The eqn (2) can be rearranged to the following form

$$\beta_{hkl}\cos\theta_{hkl} = C\varepsilon\sin\theta_{hkl} + \frac{K\lambda}{D} \quad (3)$$

which is better suited for determination of the mean crystallite size D by linear regression. In order to get the correct information about the mean grain size D determined from the peak broadening, it is necessary to correct the measured line widths β_{exp} for the instrumental contribution β_{ins}. The so-called Instrumental Resolution Function (IRF) was determined by measuring standard material LaB_6 at the same experimental and geometrical conditions as the studied material. When describing diffraction profiles by a Lorentzian profile function correction of the line widths is performed in the following way $\beta_{exp} = \beta_{exp} - \beta_{ins}$, whereas using Gaussian profiles yields the correction $\beta_{exp}{}^{2} = \beta_{exp}{}^{2} - \beta_{ins}{}^{2}$. It should be noted here that the Williams–Hall plot defined by eqn (2) is appropriate for situations when pure Lorentzian profiles are considered. If pure Gaussians profiles are considered, then all terms in eqn (2) should be squared.[28]

Results and discussion

The SBA-15 structure, prepared according to original procedure,[29] is formed by ordered 2D hexagonal channels interconnected by micropores. From the first preparation of SBA-15, several papers published some variations of synthesis resulting in change of textural properties.[30–32] In our work, we prepared the SBA-15 with pore size about 6 nm according to the typical procedure published by Zhao *et al.*[33] This pore size was confirmed by nitrogen adsorption measurements (see below). Molecule of DOX has dimensions approximately 1.5 × 0.9 nm, so it can easily enter the 6 nm large mesopores of SBA-15.

FT-IR study

Infrared spectroscopy is typically used to provide information about surface of materials for chemical groups identification. The measured spectra of samples are presented in Fig. 4. The

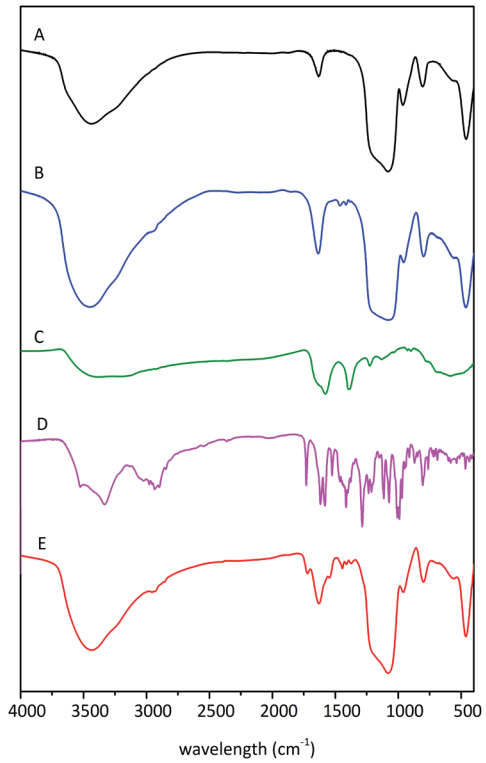

Fig. 4 FTIR spectra of the samples SBA-15 (A), rSBA-15 (B), ZnS–COOH (C), DOX (D) and DOX–rSBA-15 (E).

FT-IR spectrum of SBA-15 shows strong and broad bands in the region around 1100 cm^{-1} and 790 cm^{-1}, which are ascribed to the asymmetric ν_{as} (Si–O–Si) and symmetric ν_{s} (Si–O–Si) stretches of SBA-15 framework. The presence of bending vibration δ(Si–O–Si) at about 460 cm^{-1} is another sign of siliceous network. The deformation vibrations of water are manifested at the spectrum as a band around 1620 cm^{-1}. Also, the stretching vibrations of water and silanol groups are represented as a broad band in the range 3750–3000 cm^{-1}. The infrared spectra of the rSBA-15 and DOX–rSBA-15 have the same bands as SBA-15 so only main differences will be discussed. The modification of the surface by amino-disulphide groups results in new bands observed in the range 1500–1350 cm^{-1}, which are ascribed to the δ(NH) and $\delta(CH_2)$ bending vibrations.[34] Moreover, the bands in the region around 2900 cm^{-1}, correspond to the ν (C–H) stretching vibrations of aliphatic chain.

The FTIR spectrum in Fig. 4C, corresponding to ZnS–COOH nanoparticles confirms the presence of –COOH groups on the surface by the bands of ν_{CO_2} asymmetric stretch at around 1577 cm^{-1}, ν_{CO_2} symmetric stretch at around 1396 cm^{-1} and ν_{C-O} stretch at 1224 cm^{-1}.[35] The bands around 800–600 cm^{-1} indicate the presence of C–S bond. The bonding of –COOH groups on the surface of ZnS was proven by the absence of bands characteristic for S–H in the region 2600–2500 cm^{-1}.

The infrared spectra of DOX–rSBA-15 showed characteristic bands of all three previously discussed materials and moreover new bands, which can be attributed to the presence of doxorubicin, were observed. The presence of carbonyl group of

doxorubicin can be confirmed by the band at about 1700 cm^{-1}. Furthermore, there are more pronounced ν (C–H) stretching vibrations at about 2900 cm^{-1}.

TGA and elemental study

To obtain the information about the amount of adsorbed DOX and surface-bonded organic groups, the thermogravimetric and elemental analysis were conducted. Fig. 5A shows TG curves of SBA-15-Cl, rSBA-15 and DOX–rSBA-15. The successful attachment of chemical groups, ZnS–COOH NPs and loading of DOX was proved by the increase of weight percentage loss after each synthetic step. The mass decrease to around 200 °C corresponds to the thermodesorption of solvents used in the synthesis. As the temperature rises above 260 °C, the 3-chloropropyl groups of SBA-15-Cl start to decompose and the decomposition stops at about 750 °C. The total mass loss of SBA-15-Cl was 8.8%. Thermogravimetric analysis of amino-disulphide modified sample in the temperature range from 215 to 800 °C shows weight loss of 17%, which corresponds to the thermal decomposition of the organic groups. This result well correlates with the elemental analysis results, which showed that the sample rSBA-15 contained 8.22% of C, thus 17% of amino-disulphide groups. Material DOX–rSBA-15 showed 23% weight loss, which is about 5.6 wt% greater than weight loss of rSBA-15. However, 5.6 wt% represents not only the amount of adsorbed DOX, but also amount of ZnS–COOH NP. Therefore, we used

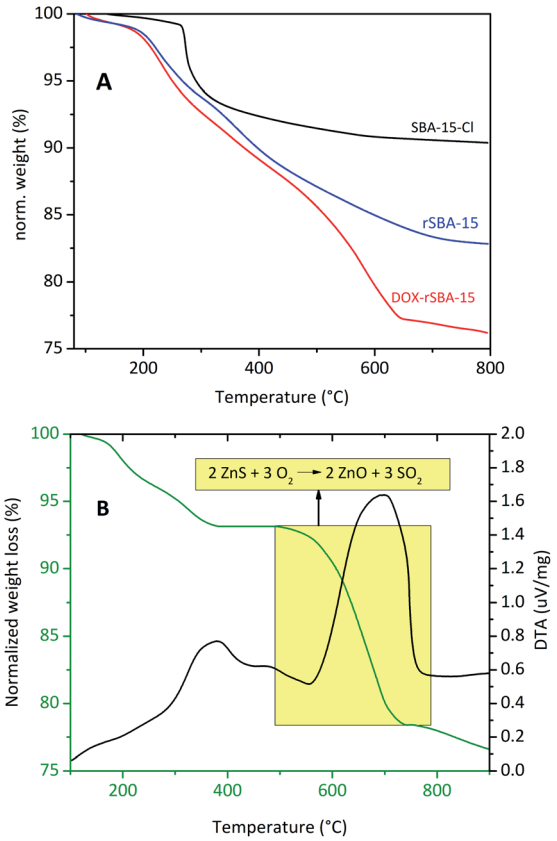

Fig. 5 TGA curves of the samples SBA-15-Cl (A, red), rSBA-15 (A, blue), DOX–rSBA-15 (A, black) and ZnS–COOH (B).

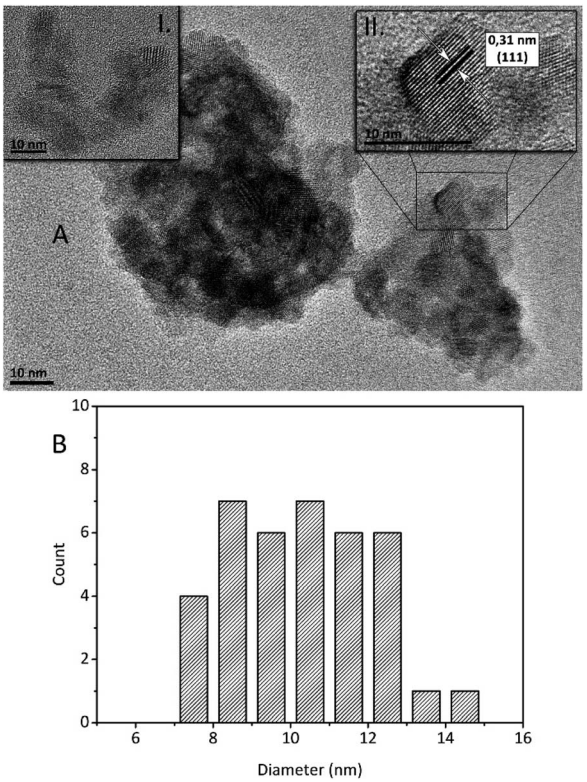

Fig. 6 HRTEM micrograph (A) and crystal size distribution (B) of ZnS–COOH NPs.

elemental analysis (CHN) to find the weight distribution between DOX and ZnS–COOH NP. According to elemental analysis results, the sample DOX–rSBA-15 contains about 4.7 wt% more sulphur, compared to rSBA-15. So, the 4.7 wt% of sulphur is attributed to the ZnS–COOH NPs. Adsorbed amount of DOX was than calculated to be 2.49 wt%.

Thermal analysis was measured also for synthesised ZnS–COOH nanoparticles (see Fig. 5B). TGA curves in Fig. 5B showed 6.4% weight loss from 100 °C to 400 °C, which was assigned to release of surface organic moieties (carboxyls). Further weight loss (14.8 wt%) corresponds to transformation of ZnS to ZnO and release of sulphur dioxide.

The structural analysis of ZnS–COOH NPs was also made by HRTEM images (see Fig. 6A). Prepared ZnS–COOH NPs have cubic ZnS structure, which was proved by the lattice spacing of 0.31 nm shown on the upper right inset of Fig. 6A. The mean diameter of ZnS–COOH NPs crystals was estimated from HRTEM images and the result was depicted in Fig. 6B. The particles were rather agglomerated however, it was possible to find the areas of non-agglomerated particles and these were used for size distribution analysis (see upper left inset in Fig. 6A). The smallest NPs have size around 7 nm and the largest ones have 14 nm in diameter. The most abundant diameter was around 8 nm and 10 nm, and the mean crystal size was calculated at 10.4 nm.

Textural properties, TEM and XRD

The textural characteristics of prepared samples were characterized by nitrogen adsorption/desorption at 77 K. The

isotherms and calculated BJH pore size distribution plots are depicted in Fig. 7. The isotherm shape for SBA-15 and rSBA-15 is characteristic of mesoporous materials with periodic 2D hexagonal pore arrangement. The steep increase of volume of adsorbed nitrogen at about $p/p_0 = 0.7$ for SBA-15 suggests the uniform pore size distribution of SBA-15. The claim was also supported by the narrow pore size distribution on the BJH graph in Fig. 7B, the pore size of SBA-15 was about 5.9 nm.

A small shift of capillary condensation to the lower relative pressure as well as reduced amount of adsorbed volume of N_2 was observed for r-SBA-15 and DOX–rSBA-15 samples, which is the sign of successful surface modification by amino-disulphide moieties and filling of the pores by loaded species.

The desorption isotherms for materials SBA-15 and rSBA-15 didn't follow the adsorption isotherms path and the desorption is delayed. This leads to the hysteresis, with adsorption and desorption branches of the isotherms parallel, which is another sign of mesoporous morphology with channel-like pores. The hysteresis loop for materials SBA-15 and rSBA-15 closes in the relative pressures about 0.6 and 0.5, respectively. Moreover, for rSBA-15, a decrease of pore diameter was observed in comparison with pure SBA-15 sample (4.9 nm for rSBA-15 and 5.9 nm for SBA-15). The isotherms for SBA-15 and rSBA-15 can be characterized as of IVa type according to the IUPAC classification, *i.e.* hysteresis loop H1.[36] For sample DOX–rSBA-15 a different shape of the hysteresis loop was observed. The hysteresis loop of DOX–rSBA-15 can be characterized as of IV a type, hysteresis loop H2, with triangular shape.[37]

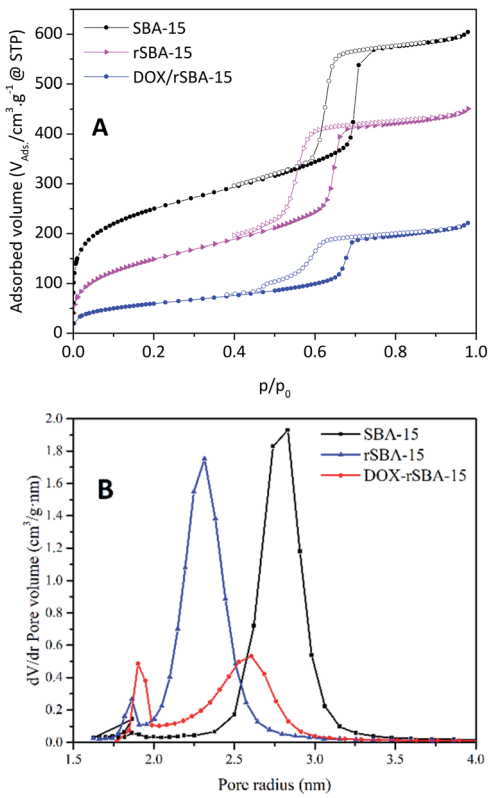

Fig. 7 BET isotherms (A) and BJH pore size distribution (B) of samples SBA-15 (square), r-SBA-15 (triangle) and DOX–rSBA-15 (circle).

Table 1 Calculated textural characteristics of SBA-15, rSBA-15 and DOX–rSBA-15

Sample	BET surface area (m^2 g^{-1})	Pore volume (cm^3 g^{-1})	Pore diameter (Å)
SBA-15	908	0.73	59
rSBA-15	549	0.66	49
DOX–rSBA-15	217	0.36	54

The change in the hysteresis loop indicates the partial filling of the pores by DOX molecules and change of the pore diameter as suggested in ref. 38. Moreover, the change in the hysteresis loop can be due to the attachment of ZnS–COOH nanoparticles on the pore entries, which results in narrower pore size at some pores.[38] This suggestion is also supported by pore size distribution, where two different pore sizes were detected for DOX–rSBA-15 sample (see Fig. 7B). From these results we suppose that ZnS–COOH nanoparticles don't cover all the pore entries of silica and this hypothesis was further confirmed by STEM results.

The loading of DOX and pore capping by ZnS–COOH nanoparticles are reflected by the further decrease of surface area and adsorbed volume of nitrogen (see Table 1). There is also change of isotherm profile, where the capillary condensation step shows gradual ascend and is not as steep as can be seen for SBA-15. This change can be ascribed to uncomplete pore capping and uneven spread of DOX across the DOX–rSBA-15 nanomaterial. The all computed textural parameters are summarized in Table 1. The morphology and structure of the prepared samples was also confirmed by STEM. The STEM micrograph of rSBA-15, shown in Fig. 8, clearly demonstrate the ordered hexagonal arrays of the one-dimensional channels even after functionalization. The ZnS–COOH nanoparticles can be

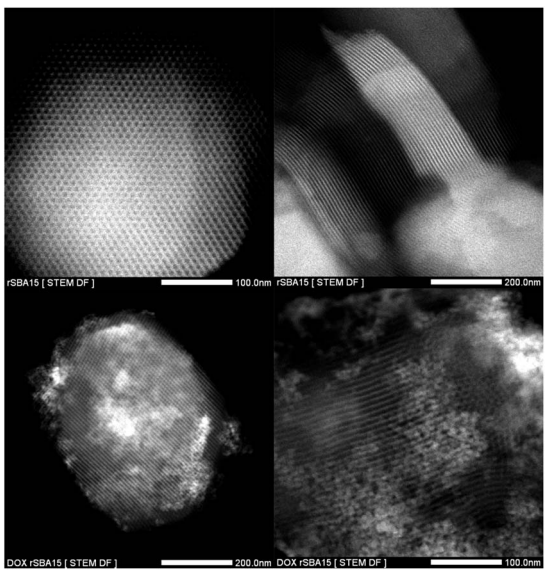

Fig. 8 TEM images of rSBA-15 (upper two micrographs) and DOX–rSBA-15 (lower two micrographs) at different magnifications.

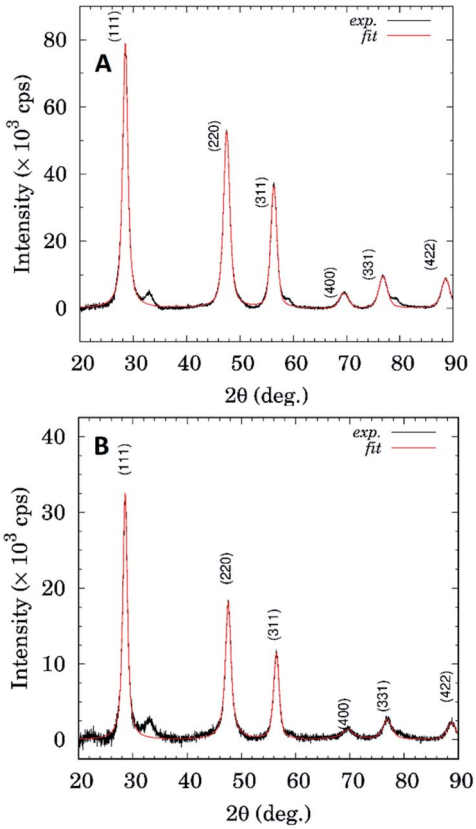

Fig. 9 Comparison of XRD patterns for ZnS–COOH (A) and DOX–rSBA15 (B) samples.

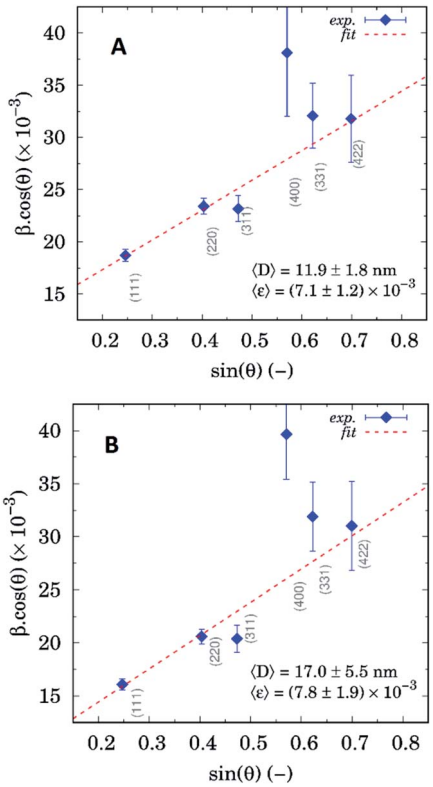

Fig. 10 William–Hall plots based on diffraction profile analysis for ZnS–COOH (A) and DOX–rSBA-15 (B).

observed as small particles on the external surface of mesoporous silica. As can be seen, the ZnS–COOH nanoparticles don't cover all the pore entries of silica.

Fig. 9 shows comparison of XRD patterns for the sample ZnS–COOH and DOX–rSBA15. It seems that both samples show presence of the ZnS cubic phase (sphalerite). The ZnS–COOH sample shows only higher scattering intensity, otherwise phase composition is the same as in the case of the DOX–rSBA sample. As can be seen from Fig. 9, XRD profiles for both samples show rather broad diffraction profiles, which is a fingerprint of their nanocrystalline microstructure.

Diffraction profile analysis based on William–Hall method (see Fig. 10) yields mean crystallite sizes 11.9 ± 1.8 nm and 17.0 ± 5.5 nm for ZnS–COOH and DOX–rSBA15 samples, respectively.

UV-VIS analysis

UV-VIS spectrum of ZnS–COOH NPs is shown in Fig. 11. By using the Tauc equation we determined the optical band gap energy of nanoparticles:

$$(\alpha h\nu)^n = A(h\nu - E_g)$$

where, "α" is absorption coefficient, "$h\nu$" is incident photon energy, "A" is a proportionality constant and "n" determines the degree of transition and its typical values are 1/2, 3/2, 2 or 3 for allowed direct, forbidden direct, allowed indirect and forbidden indirect transitions, respectively.[39] Typical optical band gap energy for bulk ZnS is 3.6 eV.[40] The best fit was obtained for $n = 1/2$, suggesting allowed direct transition of ZnS–COOH NPs. The extrapolated value gave the $E_g = 3.68$ eV.

Zeta potential measurements

To determine the electro-kinetic charge of the prepared materials the zeta potential measurements were performed in

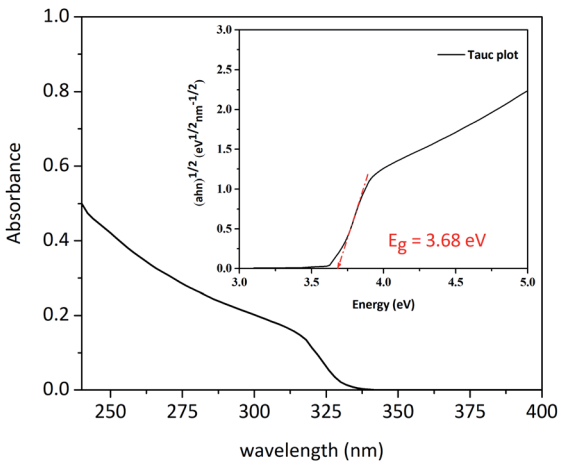

Fig. 11 UV-VIS graph of ZnS–COOH NPs and calculated Tauc plot.

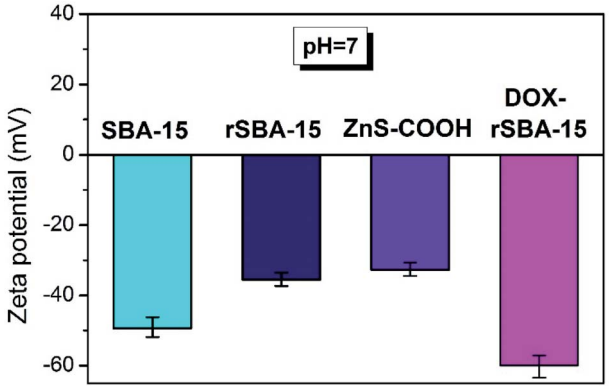

Fig. 12 Zeta potential of the studied carriers measured at pH = 7.4.

aqueous suspensions at pH = 7.4 (see Fig. 12). The respective zeta potential value was determined as an average of 40 scans. For the pure, unmodified sample SBA-15 the negative value of zeta potential approximately −49.3 mV was recorded at pH = 7.4, corresponding to progressive dissociation of Si–OH groups. Observed value is in good agreement with the data obtained for other silica-based surfaces.[41–43] The effect of amine modification and presence of amine groups in the redox responsive rSBA-15 structure is reflected by negative zeta potential values of −35.5 mV. For pure ZnS–COOH nanoparticles, the value of zeta potential −32.7 mV at pH = 7.4 was observed. With loading of doxorubicin (DOX) and capping ZnS–COOH NPs in redox responsive rSBA-15 matrix, the zeta potential becomes more negative as a result of progressive dissociation of amine groups, reaching the value of −59.4 mV. Also, the loading of doxorubicin (DOX), as a weak acid, has effect on the surface charge due to formation of intermolecular interactions and proton exchange between molecules of drugs and amine groups. The presence of mentioned interactions was reflected by the decrease of zeta potential value in final sample DOX–rSBA-15 (see Fig. 12).

Magnetic study

ZnS is a well-known II–VI semiconductor with wide direct bandgap of 3.72 eV for cubic zinc blende (sphalerite) and 3.77 eV for hexagonal wurtzite. A wide band gap in ZnS gives the opportunity to appear the hole-mediated ferromagnetism after substitution of Zn by 3d ions. From magnetic point of view, the un-doped bulk ZnS material is known as diamagnetic with a listed value of magnetic susceptibility -2.6×10^{-7} emu g^{-1} Oe^{-1}.[44,45] Besides the typical diamagnetic behaviour in bulk ZnS crystals, with decreasing of particles size to nanometer range and with doping (Mn, Co, Fe), the paramagnetic or weak ferromagnetic behaviour was reported.[44,45]

To investigate the magnetic properties of ZnS–COOH nanoparticles in DOX–rSBA-15 sample, the magnetization (magnetic moment per mass) in ZFC/FC regimes was measured in the range of 1.8–300 K under the external magnetic field of 10 kOe, see Fig. 13A. The ZFC was performed by cooling the sample under no magnetic field and the magnetization was measured with the increasing temperature in 10 000 Oe of magnetic field,

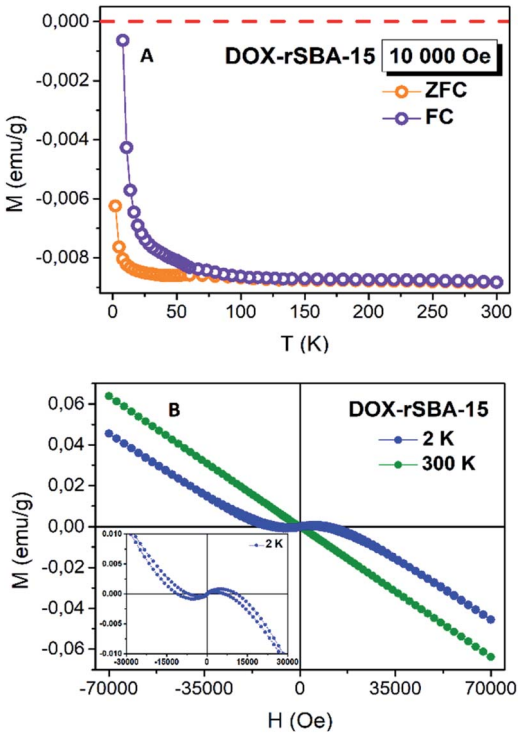

Fig. 13 (A) Magnetization *versus* temperature measured in ZFC (violet) and FC (orange) regimes in pure ZnS–COOH nanoparticles in external magnetic field of 10 000 Oe. (B) Magnetization *versus* magnetic field measured at 300 K (green) and 2 K (blue colour). Inset is detail on irreversibility of magnetization curve estimated at 2 K.

whereas the FC curve was taken in the field of 10 000 Oe with the decreasing temperature. Besides of a gradual increase of the magnetization with the decreasing temperature was observed, the negative values of magnetization confirm the diamagnetic features. The opposite, the separation of ZFC/FC curves reveals a typical behaviour of ferromagnetism. This is consistent with the result of the $M(H)$ measurements at $T = 300$ K, and $T = 2$ K, see Fig. 13B. It is clearly seen that the sample DOX–rSBA-15 at 2 K exhibits a mixed behaviour of diamagnetic and ferromagnetic. The observed magnetic behaviour falls in the topic so called novel magnetism. Nanostructured materials often show different magnetic behaviour than their bulk counterparts. Materials, which are diamagnetic in the bulk show magnetic properties in nanoscale. This behaviour is often induced by structural defects, atom vacancies.[45,46] The appearing of the ferromagnetism may be ascribed to the existence of the sulphur vacancies and zinc interstitials. This feature agrees with results published in ref. 45 and confirms the nano-range character of prepared ZnS–COOH in the structure of DOX–rSBA-15. The results showed that the designed cargo system DOX–rSBA-15 can be easily monitored using magnetic measurements which open possibilities of use of such drug delivery system as theranostic agent.

Release study

The redox responsive behaviour of DOX–rSBA-15 was studied in two different media, physiological saline solution with 10 mM

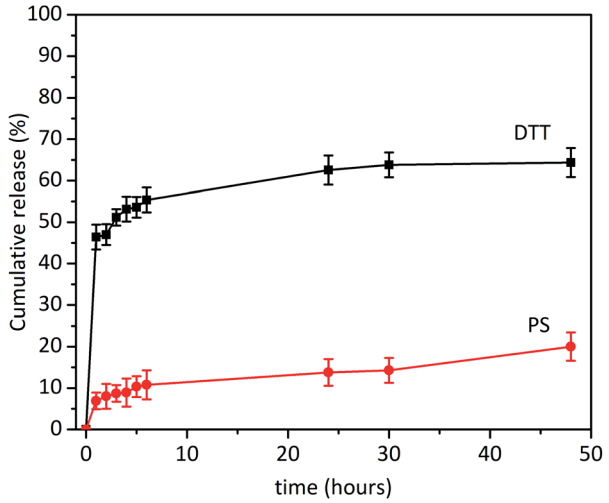

Fig. 14 *In vitro* release profiles of DOX–rSBA-15 in the media with a DTT and in the physiological saline solution (PS).

concentration of DTT and physiological saline with pH of 7.4 (*i.e.* without DTT). Three independent release measurements were made, and the respective value was obtained as an average of these measurements. Calculated cumulative release curves are depicted in Fig. 14. The sampling was done in time intervals of 1, 2, 3, 4, 5, 6, 24, 30 and 48 hours. The results showed that lower DOX release was observed in media without DTT (see PS curve in Fig. 14). As it was observed in TEM images in Fig. 8, not all pores of SBA-15 are capped with ZnS nanoparticles, which cause partial release in media even without the presence of DTT. This was evidenced by release of DOX in the first hour (6.89%) followed by the gradual diffusion release to the final 20.01% of DOX after 48 hours.

However, after addition of 10 mmol of DTT, the pores of the sample DOX–rSBA-15 were unblocked due to redox cleavage of S–S bond and larger release of DOX was observed (see DTT curve in Fig. 14). The largest amount of DOX was released during first hour (46.44%). After this time the slope of the release curve changed, and the release slowed down. In first 24 hours 63.5% of loaded DOX was released. In the time interval above 24 hours the release was negligible and only 2% of DOX was released in the period between 24 and 48 hours. It can be seen, that DOX was not released quantitively and after 48 hours only 64.36% of DOX was released. We suppose that carboxylic and OH groups of DOX can interact by non-covalent interactions with surface of SBA-15 [47] and after 48 hours, an equilibrium was reached between DOX bound to the surface of SBA-15 and released DOX.

In the context of the release study, the question of cytotoxicity of the prepared cargo system can arise. We showed in our previous studies,[4,48] that pure silica nanoparticles as well as organic ligand-modified silica nanoparticles has no cytotoxicity. However, when anticancer drug was loaded into the silica nanoparticles, the delivery system showed significant cytotoxic effects on human glioma U87 MG cells.[4,48] As for ZnS nanoparticles, we did not investigate their cytotoxicity. However, the literature data show, that at low concentrations ZnS nanoparticles have no toxic effects *e.g.* on lymphocytes[49,50] or *e.g.* mouse RPE cells.[51] This is advantage of the use of ZnS nanoparticles instead of CdS particles used in other studies.[16]

Conclusions

In summary a redox responsive drug delivery system was successfully designed and constructed by capping ZnS–COOH NP on the surface of the functionalized mesoporous silica rSBA-15. The DOX, as a model anticancer drug, was encapsulated into the pores of rSBA-15 and the pores were capped by the ZnS–COOH NPs. The *in vitro* drug release demonstrated, that the DOX could be entrapped with a low leakage in the absence of redox molecule such as DTT, which as a result have potential to protect the healthy cells during drug delivery to the site of an action. In the presence of DTT, the release of DOX significantly increased owing to the cleavage of the disulphide bonds. The result of this work proved that rSBA-15 with ZnS–COOH as a capping agent could be considered as a smart drug carrier for redox-responsive drug-controlled release. Moreover, optimisation of ZnS concertation can lead to better tightness of the designed system (some pores of rSBA-15 were non capped in our study) and consequently lower premature release. The possibility of detection of the ZnS–COOH nanoparticle caps in DOX–rSBA-15 sample by magnetic field opens the potential of the use of such system in theranostic applications.

Conflicts of interest

There are no conflicts to declare.

Acknowledgements

This work was supported by the Slovak Research and the Development Agency under the contracts APVV-15-0520 and bilateral grant APVV-SK-FR-2017-0011. The authors V. Z. and A. Z. thank the Ministry of Education, Science, Research and Sport of the Slovak Republic and the Accreditation Commission for the financial support of the TRIANGEL team in the frame of the scheme "Top Research Teams in Slovakia". Moreover, the work was supported by the Development Operational Programme Research and Innovation for the project "New unconventional magnetic materials for applications (NEMMA)", ITMS: 313011T544, co-funded by the European Regional Development Fund (ERDF).

References

1 H. Ritchie and M. Roser, *Causes of Death. Our World in Data*, published online at OurWorldInData.org. retrieved from: https://ourworldindata.org/causes-of-death, accessed October 2019.
2 C. A. Lipinski, Poor aqueous solubility—an industry wide problem in drug discovery, *Am. Pharm. Rev.*, 2002, **5**, 82.
3 E. M. Merisko-Liversidge and G. G. Liversidge, Drug nanoparticles: formulating poorly water-soluble compounds, *Toxicol. Pathol.*, 2008, **36**, 43.

4 E. Beňová, D. Bergé-Lefranc, V. Zeleňák, M. Almáši, V. Huntošová and V. Hornebecq, Adsorption properties, the pH-sensitive release of 5-fluorouracil and cytotoxicity studies of mesoporous silica drug delivery matrix, *Appl. Surf. Sci.*, 2020, **504**, 144028.
5 M. Yu, S. Jambhrunkar, P. Thorn, J. Chen, W. Gu and C. Yu, Hyaluronic acid modified mesoporous silica nanoparticles for targeted drug delivery to CD44-overexpressing cancer cells, *Nanoscale*, 2013, **5**, 178.
6 D. Dheer, J. Nicolas and R. Shankar, Cathepsin-sensitive nanoscale drug delivery systems for cancer therapy and other diseases, *Adv. Drug Delivery Rev.*, 2019, **151–152**, 130.
7 Q. Zhao, C. Wang, Y. Liu, J. Wang, Y. Gao, X. Zhang, T. Jiang and S. Wang, PEGylated mesoporous silica as a redox-responsive drug delivery system for loading thiol-containing drugs, *Int. J. Pharm.*, 2014, **477**, 613.
8 A. Sharma, E. J. Kim, H. Shi, J. Y. Lee, B. G. Chung and J. S. Kim, Development of a theranostic prodrug for colon cancer therapy by combining ligand-targeted delivery and enzyme-stimulated activation, *Biomaterials*, 2018, **155**, 145.
9 D. He, X. He, K. Wang, J. Cao and Y. Zhao, A light-responsive reversible molecule-gated system using thymine-modified mesoporous silica nanoparticles, *Langmuir*, 2012, **28**, 4003.
10 L. Mahlert, J. Anderski, T. Schoppa, D. Mulac, J. Sun, D. Kuckling and K. Langer, In vitro evaluation of innovative light-responsive nanoparticles for controlled drug release in intestinal PDT, *Int. J. Pharm.*, 2019, **565**, 199.
11 W. Zhao, B. Cui, H. Qiu, P. Chen and Y. Wang, Multifunctional Fe_3O_4@WO_3@mSiO_2–APTES nanocarrier for targeted drug delivery and controllable release with microwave irradiation triggered by WO_3, *Mater. Lett.*, 2016, **169**, 185.
12 T. Boissenot, A. Bordat, E. Fattal and N. Tsapis, Ultrasound-triggered drug delivery for cancer treatment using drug delivery systems: from theoretical considerations to practical applications, *J. Controlled Release*, 2016, **241**, 144.
13 M. Moros, J. Idiago-López, L. Asín, E. Moreno-Antolín, L. Beola, V. Grazú, R. M. Fratila, L. Gutiérrez and J. Martínez de la Fuente, Triggering antitumoural drug release and gene expression by magnetic hyperthermia, *Adv. Drug Delivery Rev.*, 2019, **138**, 326.
14 A. Kumar, J. White, R. J. Christie, N. Dimasi and C. Gao, Chapter twelve - antibody-drug conjugates, *Annu. Rep. Med. Chem.*, 2017, **50**, 441.
15 H. Labiadh, K. Lahbib, S. Hidouri, S. Touil and T. B. Chaabane, Insight of ZnS nanoparticles contribution in different biological uses, *Asian Pac. J. Trop. Med.*, 2016, **9**, 757.
16 C. Y. Lai, B. G. Trewyn, D. M. Jeftinija, K. Jeftinija, S. Xu, S. Jeftinija and V. S. Lin, A mesoporous silica nanosphere-based carrier system with chemically removable CdS nanoparticle caps for stimuli-responsive controlled release of neurotransmitters and drug molecules, *J. Am. Chem. Soc.*, 2003, **125**, 4451.
17 S. Giri, B. G. Trewyn, M. P. Stellmaker and V. S. Lin, Stimuli-responsive controlled-release delivery system based on mesoporous silica nanorods capped with magnetic nanoparticles, *Angew. Chem., Int. Ed. Engl.*, 2005, **44**, 5038.
18 F. Torney, B. G. Trwyn, V. S. Lin and K. Wang, Mesoporous silica nanoparticles deliver DNA and chemicals into plants, *Nat. Nanotechnol.*, 2007, **2**, 295.
19 Ch. L. Zhu, Ch. H. Lu, X. Y. Song, H. H. Yang and X. R. Wang, Bioresponsive controlled release using mesoporous silica nanoparticles capped with aptamer-based molecular gate, *J. Am. Chem. Soc.*, 2011, **133**, 1278.
20 F. Muhammad, W. Qi, A. Wang, J. Gu, J. Du and G. Zhu, Using oxidant susceptibility of thiol stabilized nanoparticles to develop an inflammation triggered drug release system, *J. Mater. Chem. B*, 2015, **3**, 1597.
21 W. H. Zhang, J. L. Shi, H. R. Chen, Z. L. Hua and D. S. Yan, Synthesis and characterization of nanosized ZnS confined in ordered mesoporous silica, *Chem. Mater.*, 2001, **13**, 648.
22 Y. Du, Y. Fu, X. Guo, H. Li, Ch. Lü and Z. Su, Fabrication of fluorescent mesoporous silica nanoparticles with confined 8-hydroxyquinoline functionalized ZnS nanoparticles and their transparent polymer nanocomposites, *Microporous Mesoporous Mater.*, 2010, **130**, 122.
23 C. Liu, Y. Ji and T. Tan, One-pot hydrothermal synthesis of water-dispersible ZnS quantum dots modified with mercaptoacetic acid, *J. Alloys Compd.*, 2013, **570**, 23.
24 D. Halamová, M. Badaničová, V. Zeleňák, T. Gondová and U. Vainio, Naproxen drug delivery using periodic mesoporous silica SBA-15, *Appl. Surf. Sci.*, 2010, **256**, 6489.
25 C. A. Schneider, W. S. Rasband and K. W. Eliceiri, NIH Image to ImageJ: 25 years of image analysis, *Nat. Methods*, 2012, **9**, 671.
26 P. Scherrer, Bestimmung der inneren struktur und der größe von kolloidteilchen mittels röntgenstrahlen, in *Kolloidchemie Ein Lehrbuch*, ed. R. Zsigmondy, Springer, Berlin, Heidelberg, 1912, pp. 387–409.
27 G. K. Williamson and W. H. Hall, X-ray line broadening from filed aluminium and wolfram, *Acta Metall.*, 1953, **1**, 22.
28 D. L. Dorset, X-ray Diffraction: a practical approach, *Microsc. Microanal.*, 1998, **4**, 513.
29 D. Zhao, J. Feng, Q. Huo, N. Melosh, G. H. Fredrickson, B. F. Chmelka BF and G. D. Stucky, Triblock copolymer syntheses of mesoporous silica with periodic 50 to 300 Angstrom pores, *Science*, 1998, **279**, 548.
30 A. Sayari, B. H. Han and Y. Yang, Simple synthesis route to monodispersed SBA-15 silica rods, *J. Am. Chem. Soc.*, 2004, **126**, 14348.
31 A. Katiyar, S. Yadav, P. G. Smirniotis and N. G. Pinto, Synthesis of ordered large pore SBA-15 spherical particles for adsorption of biomolecules, *J. Chromatogr. A*, 2006, **1122**, 13.
32 A. Carrero, J. Moreno, J. Aguado J and G. Calleja, Control of SBA-15 materials morphology by modification of synthesis conditions, in *Studies in Surface Science and Catalysis*, ed. A. Gédéon, P. Massiani and F. Babonneau, Elsevier, 2008, vol. 174 part A, pp. 321–324.
33 D. Zhao, Q. Huo, J. Feng, B. F. Chmelka and G. D. Stucky, Nonionic triblock and star diblock copolymer and oligomeric surfactant syntheses of highly ordered,

hydrothermally stable, mesoporous silica structures, *J. Am. Chem. Soc.*, 1998, **120**, 6024.

34 T. Yokoi, H. Yoshitake and T. Tatsumi, Synthesis of amino-functionalized MCM-41 *via* direct co-condensation and post-synthesis grafting methods using mono-, di- and tri-amino-organoalkoxysilanes, *J. Mater. Chem.*, 2004, **14**, 951.

35 J. J. Max and C. Chapados, Infrared spectroscopy of aqueous carboxylic acids: comparison between different acids and their salts, *J. Phys. Chem. A*, 2004, **108**, 3324.

36 J. Rouquerol, D. Avnir, C. W. Fairbridge, D. H. Everett, J. M. Haynes, N. Pernicone, J. D. F. Ramsay, K. S. W. Sing and K. K. Unger, Recommendations for the characterization of porous solids (Technical Report), *Pure Appl. Chem.*, 1994, **66**, 1739.

37 M. Thommes, K. Kaneko, A. V. Neimark, J. P. Olivier, F. R. Reinoso, J. Rouquerol and K. S. W. Sing, Physisorption of gases, with special reference to the evaluation of surface area and pore size distribution (IUPAC Technical Report), *Pure Appl. Chem.*, 2015, **87**, 1051.

38 V. Zeleňák V, A. Zeleňáková, J. Kováč, U. Vainio and N. Murafa, Influence of surface effects on magnetic behavior of hematite nanoparticles embedded in porous silica matrix, *J. Phys. Chem. C*, 2009, **113**, 13045.

39 B. D. Viezbicke, S. Patel, B. E. Davis and D. P. Birnie, Evaluation of the Tauc method for optical absorption edge determination: ZnO thin films as a model system, *Phys. Status Solidi B*, 2015, **252**, 1700.

40 S. D. Sartale, B. R. Sankapal, M. Lux-Steiner and A. Ennaoui, Preparation of nanocrystalline ZnS by a new chemical bath deposition route, *Thin Solid Films*, 2005, **480–481**, 168.

41 M. Colilla, I. Izquierdo-Barba, S. Sánchez-Salcedo, J. L. G. Fierro, J. L. Hueso and M. Vallet-Regí, Synthesis and characterization of zwitterionic SBA-15 nanostructured materials, *Chem. Mater.*, 2010, **22**, 6459.

42 V. Zeleňák, D. Halamová, M. Almáši, L. Žid, A. Zeleňáková and O. Kapusta, Ordered cubic nanoporous silica support MCM-48 for delivery of poorly soluble drug indomethacin, *Appl. Surf. Sci.*, 2018, **443**, 525.

43 J. M. Rosenholm and M. Lindén, Towards establishing structure–activity relationships for mesoporous silica in drug delivery applications, *J. Controlled Release*, 2008, **128**, 157.

44 S. Kumar and N. K. Verma, Room temperature magnetism in cobalt-doped ZnS nanoparticles, *J. Supercond. Novel Magn.*, 2015, **28**, 137.

45 A. Shan, W. Liu, R. Wang and C. Chen, Magnetism in undoped ZnS nanotetrapods, *Phys. Chem. Chem. Phys.*, 2013, **15**, 2405.

46 V. Zeleňák, A. Zeleňáková and J. Kováč, Insight into surface heterogenity of SBA-15 silica: oxygen related defects and magnetic properties, *Colloids Surf., A*, 2010, **357**, 97.

47 S. Björklund and V. Kocherbitov, Alcohols react with MCM-41 at room temperature and chemically modify mesoporous silica, *Sci. Rep.*, 2017, **7**, 9960.

48 M. Almáši, E. Beňová, V. Zeleňák, B. Madaj, V. Huntošová, J. Brus, M. Urbanová, J. Bednarčík and V. Hornebecq, Cytotoxicity study and influence of SBA-15 surface polarity and pH on adsorption and release properties of anticancer agent pemetrexed, *Mater. Sci. Eng., C*, 2020, **109**, 110552.

49 H. Li, M. Li, W. Y. Shih, P. I. Lelkes and W. H. Shih, Cytotoxicity tests of water soluble ZnS and CdS quantum dots, *J. Nanosci. Nanotechnol.*, 2011, **11**, 3543.

50 S. K. Dash, T. Ghosh, S. Roy, S. Chattopadhyay and D. Das, Zinc sulfide nanoparticles selectively induce cytotoxic and genotoxic effects on leukemic cells: involvement of reactive oxygen species and tumor necrosis factor alpha, *J. Appl. Toxicol.*, 2014, **34**, 1130.

51 K. Bose, H. Lakshminarasimhan, K. Sundar and T. Kathiresan, Cytotoxic effect of ZnS nanoparticles on primary mouse retinal pigment epithelial cells, *Artif. Cells, Nanomed., Biotechnol.*, 2016, **44**, 1764.